Computational Algorithm for Modeling and Correction of Gradient Nonlinearity Distortions in Magnetic Resonance Imaging

Tom S. Lee, Keith E. Schubert, Reinhard W. Schulte *

Abstract—**Targeting of brain tumors or diseased brain tissues with neurosurgical instruments or radiosurgery beams requires magnetic resonance image (MRI) sets with high spatial resolution. In recent years, the spatial resolution of MRI scanners has increased considerably with the introduction of high-field (3T) technology. As a result, isotropic submillimeter voxel sizes are more commonly being used for medical procedures. On the other hand, gradient nonlinearities introduce geometric distortions and errors into the image data. As MRI technologies continue to progress, this problem has not been resolved. We have developed a gradient nonlinearity correction method based on a cubic phantom MRI data set. The approach utilizes a sum of spherical harmonics to model the geometrically warped planes of the cube. Once the polynomial parameters are known they can be applied to correct arbitrary image sets acquired with the same scanner. In this paper, we give a detailed description of the Matlab software performing the modeling and correction functions and discuss the possibility to accelerate the code using General-Purpose Computing on Graphics Processing Units (GPGPU) techniques.**

Keywords: Magnetic Resonance Imaging, Distortion Correction Algorithm, Matlab, and Functional Radiosurgery.

1 Introduction

We describe the implementation of a software-based method to correct gradient nonlinearity distortion in Magnetic Resonance Imaging (MRI), to provide submillimeter accuracy in localization of anatomical regions for functional radiosurgery. Although current methods are successful in handling gradient nonlinearity distortion [1, 2, 3], none provide the high level of geometric accuracy required to *confidently* perform high-precision functional radiosurgery on brain targets. We have developed a software package for a phantom-based distortion method originally suggested by Langlois, et al. [4]. This report describes the structure and implementation of the code, as well as first results of its performance in stereotactic localization.

*Tom S. Lee, Software Engineer, PerMedics, Inc., 1475 South Victoria Ct., San Bernardino, CA 92408 Tel. 909-478-5000 x225 Email: tlee@permedics.com. Keith E. Schubert, Associate Professor, Dept. of Computer Science & Engineering, California State University San Bernardino, 5500 University Pkwy., San Bernardino, CA 92407 Tel. 909-537-5328 Email: schubert@csci.csusb.edu. Reinard W. Schulte, Associate Professor, Dept. of Radiation Medicine, Loma Linda University Medical Center, 11234 Anderson St., Loma Linda, CA 92354 Tel. 909-558-4243 Email: rschulte@dominion.llumc.edu.

2 Materials and Methods

2.1 Phantoms and Stereotactic Equipment

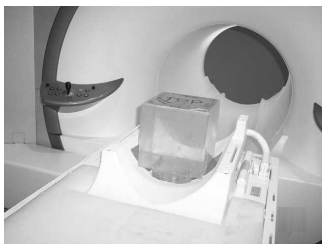

(a) Cube phantom.

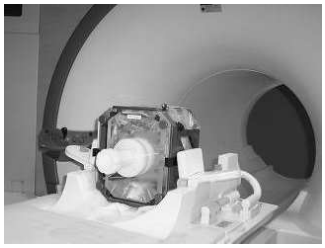

(b) Lucy® phantom.

Figure 1: Phantoms in Siemens Sonata MRI scanner.

MRI data sets of two different phantoms were acquired in this work: the first phantom was used for characterizing the scanner distortion, and the second for testing and verification of the distortion correction method. The phantom utilized for distortion characterization is a Plexiglas cube filled with oil, Figure 1(a). The images obtained represent the signal response of the oil, corresponding to the interior dimensions of the phantom (159.50mm × 159.70mm × 158.11mm). The second phantom, the Lucy® quality assurance phantom (Fluke Biomedical), was placed inside a Leksell Coordinate Frame Model G and MR Indicator (Elekta, Sweden) to perform localization of 20 MRI-compatible target markers, Figure 1(b). A certified metrology laboratory inspected the marker locations. All MRI images were acquired on a 1.5 T whole body scanner (Magnetom VISION, Siemens) with a standard head coil.

The cube phantom was centered on the isocenter of the scanner with respect to its lateral and longitudinal posi-

tion to within 1mm. Due to space limitations within the head coil, the cube center had to be placed approximately 10 mm above the scanner isocenter. The Lucy® phantom was placed at approximately the center of the head coil and at three discrete longitudinal positions: at isocenter, 50mm superior to isocenter, and 50mm inferior to isocenter in order to test the accuracy of distortion-corrected localization both in the center and toward the periphery of the magnetic field.

The automated 3D calibration of the shim coils was performed to correct for B_0 field inhomogeneities prior to scanning. Two sets of sequences were performed: one with and one without internal correction for gradient nonlinearity, to compare the effectiveness of the internal scanner correction to that of the software-based MRI gradient nonlinearity distortion correction. Scan parameters for the cube phantom were as follows: 512 × 512 matrix, 0.391mm pixel size, 200mm field of view, 104 slices of 2.0mm thickness. Axial, coronal, and sagittal sequences were acquired. Scan parameters for the Lucy® phantom were as follows: 512 × 512 matrix, 0.586mm pixel size, 300mm field of view, 112 slices of 2.0mm thickness. Axial and coronal sequences were acquired. Figure 2 shows representative axial and coronal images of the Lucy® phantom, while Figure 3 shows representative axial, coronal, and sagittal images of the cube phantom.

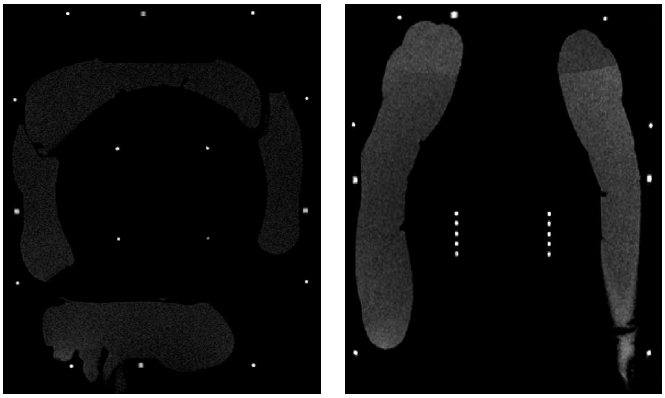

(a) Axial scan. (b) Coronal scan.

Figure 2: Example scans of Lucy® phantom, showing fiducial points (edges) used for stereotactic localization of MRI markers (center).

2.2 Computational Algorithm

The gradient nonlinearity distortion correction was written in Matlab version 7.0.4. Details of the code have been described elsewhere [5, 6, 7]. Matlab provides strong support for DICOM data types, as well as robust image processing functions and data visualization tools.

Data Quality Assurance

Prior to calculating the distortion model, the data underwent a series of image processing and quality checks. These checks had three goals: (1) eliminate as much image noise as possible, (2) remove extraneous and unwanted features in each MR image, and (3) ensure the data is accurate for future calculations.

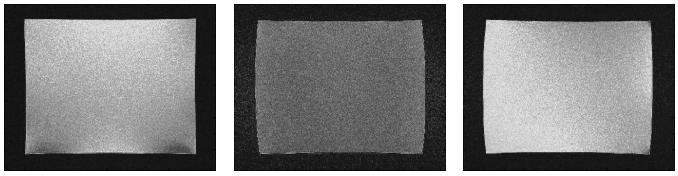

(a) Axial. (b) Coronal. (c) Sagittal.

Figure 3: Examples of useful slices of oil-filled phantom, with distortion clearly visible in the outer regions.

Selection of Useful Slices

The distortion correction was only based on slices that contained a full view of the phantom. To select useful slices such as those in Figure 3, the algorithm analyzed the distribution of pixel intensities of a slice near the center of the slab, which always contained a full view of the phantom. Using this reference slice, the algorithm compared the pixel intensities of each slice to determine the range of the study that contained the phantom. This effectively eliminated slices that do not contain the phantom, or contain a partial view of the phantom. The indexes of the first and last useful slices were reported, and slices outside this range were excluded from analysis.

Edge Detection

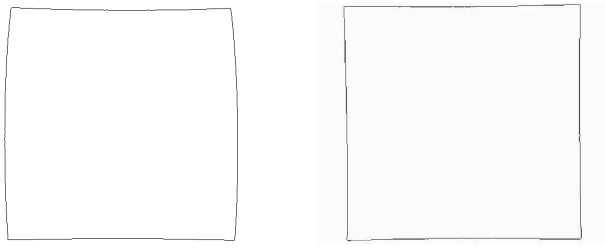

Figure 4: Representative examples of edge images.

Edge detection was performed to provide the representation of the distorted physical edges of the phantom for the gradient nonlinearity distortion correction. The Canny edge detector provided by Matlab was chosen because it was least sensitive to noise, and the edge images produced were sharper and more accurate, thus delivering the most consistent results from study to study when compared to other edge detection methods implemented in Matlab. Matlab's Canny edge detector automatically calculates a threshold for edge detection; however, this threshold considers every single intensity shift within the image, and in doing so, finds fictitious edges within the phantom. We implemented a threshold algorithm that converged on the

optimal threshold value in an iterative series of edge detection trials. The threshold algorithm used the reference slice chosen in the previous step, and automatically configured its settings (threshold increment and stop condition) based on the strength of the image gradient across the edges. Starting with Matlab's automatically calculated threshold, the threshold algorithm incremented the threshold in small successive steps (0.5 - 0.75). As the threshold was increased, the number of fictitious edges decreased, leaving only the strong image features behind. The optimal threshold was assumed when the number of edge points did not change by more than 1% over several successive iterations (5-10, depending on the stop condition). This optimized threshold was then used with Matlab's Canny edge detector on the entire set of useful slices. In an exhaustive series of tests, it was found that Canny preserved the physical edges of the phantom in the edge images, see Figure 4. The remaining unwanted image features were dealt with separately, as described below.

Removing Extraneous Features

Choosing the optimal edge detection threshold did not remove all extraneous or noisy features from the edge images. Several features were handled specifically to prepare the edge images for further calculation. The cube phantom featured a *drain plug* that allowed the phantom to be filled with oil. The hole and screw threads of the plug corrupted the edge images. A specially-designed *drain plug removal algorithm* erased the plug and drew a straight-line approximation of the affected regions. Next, the edge images were analyzed for *air bubbles*. Air bubbles within the oil adhering to the edges of the phantom created rounded defects in the edges. A *bubble removal algorithm* erased these bubbles and drew a straight-line approximation to correct the affected region. The presence of air bubbles, the drain plug, and other noisy features created minute *holes* in the edges. We implemented a *hole repair algorithm* that analyzed the four edges in all edge images for discontinuities, filling any gaps.

With these quality checks and repair algorithms, the data were ensured to be free of nearly all defects and blemishes, providing an accurate representation of the distorted phantom surfaces.

2.3 Plane Calculation

Midplanes

The correction method was based on a set of calculated "ideal" planes. These planes represented the appearance of the phantom faces without distortion. Each pair of opposite edge points in the edge images was used to calculate a midpoint. Midpoint calculation along an entire edge produced a *midline*, see Figure 5. Edge lengths could vary depending on the characteristics of the distortion in each image, so observing opposite edges of slightly different lengths was acceptable; the algorithm removed unpaired points to obtain edges of equal length. Two midlines were calculated for each edge image: one horizontal, one vertical. Due to the symmetry of gradient nonlinearity distortion, these midlines were nearly straight, providing a suitable representation of the orientation of the undistorted edges in each image, disregarding the positioning of the edges.

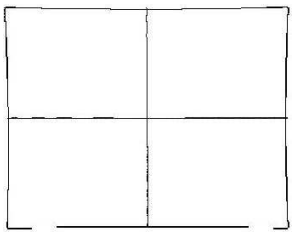

Figure 5: Calculated midlines (center horizontal and vertical straight lines) in a typical edge image.

Studies typically contained around 30,000 midpoints for each of the three pairs of phantom surfaces. The *midplane*, representing the ideal shape, size, and orientation of the particular surface of the phantom, was found by calculating the plane that resulted in the best fit of the midplane data set in the least squares sense. The Hessian normal form of a plane is: $\bar{N}^T p = d$, where $\bar{N} = [\ N_x \quad N_y \quad N_z\ ]^T$ is the normal vector to the plane with $\|\bar{N}\| = 1$, d is distance of the plane from the origin, and p is the set of vectors satisfying the plane equation. For example, fitting a plane to the top and bottom edges of the phantom in an axial study results in a plane oriented in xz. The component N_y is close to 1 in this case, so one may divide both sides of the equation by it to produce a component normalized form:

$$\begin{bmatrix} \frac{N_x}{N_y} \\ 1 \\ \frac{N_z}{N_y} \end{bmatrix}^T \begin{bmatrix} x \\ y \\ z \end{bmatrix} = \frac{d}{N_y}$$

$$\begin{bmatrix} -C_x \\ 1 \\ -C_z \end{bmatrix}^T \begin{bmatrix} x \\ y \\ z \end{bmatrix} = N^T p = C_c \qquad (1)$$

The introduction of minus signs on the coefficients, C_x and C_z, allows the equation to be easily written as $y = C_x x + C_z z + C_c$. With this form one needs to store only three components rather than four. Based on the determined orientation, the algorithm organized the data into a large $n \times 3$ matrix and a large n-element array, with n being the number of midpoints. The $n \times 3$ matrix with row vectors of the form $[\ x \quad z \quad 1\ ]$ was the *design matrix*, denoted by A, and the n-element array of y values was the *observation vector*, denoted by b. The resulting linear least squares problem was of the form $A\chi = b$ where $\chi = [\ C_x \quad C_z \quad C_c\ ]^T$ is the vector of the plane

coefficients. Solving this equation for χ yielded the midplane coefficients.

Ideal Planes

The midplanes described the correct orientation of the ideal phantom planes, but needed to be shifted along the corresponding normal vector by one-half the physical dimensions of the phantom to their correct location in 3-dimensional space. The three phantom dimensions were derived from dimensional inspection and stored prior to algorithm execution. Shifting the midplane only involved calculating a new offset term as the other coefficients must remain the same to maintain the midplane's original orientation. To calculate the offset, consider the Hessian normal form of a plane in terms of the coefficients defined in Eq. 1 and a point, $p_0 = [\ 0 \quad C_c \quad 0\ ]^T$ that lies on the midplane in our example. It is possible to determine the position of the corresponding point p_s on the shifted plane as follows:

$$p_s = \begin{bmatrix} x_s & y_s & z_s \end{bmatrix}^T = p_0 \pm \delta \bar{N} \tag{2}$$

where δ is one half the phantom dimension, and the "$\pm$" determines positive or negative shift needed to specify both ideal planes resulting from the midplane. Note that we have to use the unit vector $\bar{N} = \frac{N}{\|N\|}$ and not N in order to maintain the correct distance. Inputting p_s into the component normalized plane expression, Eq. 1, makes it possible to solve for the offset term for the shifted planes.

$$\begin{aligned} C_s &= N^T p_s \\ &= N^T(p_0 \pm \delta \bar{N}) \\ &= N^T p_0 \pm \delta N^T \bar{N} \\ &= C_c \pm \delta N^T \frac{N}{\|N\|} \\ &= C_c \pm \delta \|N\| \end{aligned} \tag{3}$$

Therefore, the offset term to obtain the ideal planes from the midplane is equal to $\delta\sqrt{C_x^2 + 1 + C_z^2}$. The same method was followed for the other planes. The result was a set of six ideal planes, one for each of the six square faces of the phantom. These ideal planes represented the faces of the phantom in the absence of gradient nonlinearity distortion.

2.4 Distortion Modeling

The final stage involved performing the actual gradient nonlinearity distortion correction. In MRI, the spatial distribution of nuclear spin density is encoded in frequency (k) space using three orthogonal gradient fields. A Fourier transform of the radiofrequency signal obtained by exciting the nuclear spins in the presence of the gradient fields yields a reconstruction of spin density in the spatial domain. Because the spatial dependence of the gradient components is nonlinear, the assumption of linearity during reconstruction results in distorted images.

The distortion model, describing the spatial dependence of the three gradient fields, was based on a finite sum of *sum of spherical harmonics* (when expressed in spherical coordinates) [2] or a sum of homogeneous polynomials (when expressed in Cartesian coordinates) [4]. Using the ideal planes obtained previously, theoretical "undistorted" data points were calculated using the ideal plane equations and acquired data points. The undistorted data points were then used to calculate the coefficients of the distortion model. Three sets of coefficients were necessary, one for each dimension. Once the model was known it was applicable to all studies performed on the particular scanner.

Let x_i, y_i, and z_i be the distorted coordinates of a point i measured by an MRI scanner. Further, let $\bar{x_i}$, $\bar{y_i}$, and $\bar{z_i}$ be the undistorted coordinates that correspond to x_i, y_i, and z_i , that is, $(\bar{x_i}, \bar{y_i}, \bar{z_i})$ is the point on the ideal plane that produced the point (x_i, y_i, z_i) in the image. Including spherical harmonics up to second order, the correction model, expressed in Cartesian coordinates, becomes [4]:

$$\begin{aligned} \alpha_i = \bar{\alpha_i} \big(1 &+ K_{\alpha_0}\left(\bar{x_i}^2 + \bar{y_i}^2\right) + K_{\alpha_1}\bar{z_i}^2 + K_{\alpha_2}\bar{z_i}^2\left(\bar{x_i}^2 + \bar{y_i}^2\right) \\ &+ K_{\alpha_3}\left(\bar{x_i}^2 + \bar{y_i}^2\right)^2 + K_{\alpha_4}\bar{z_i}^4\big) \end{aligned} \tag{4}$$

where $\alpha = (x, y, z)$. Note that all the terms in these equations are known except the K_{x_j}, K_{y_j}, and K_{z_j} terms–the desired distortion parameters. Solving for the K_{x_j} requires using the ideal planes whose normal is in the x direction, i.e., the yz planes, and similarly for the K_{y_j} and K_{z_j} terms. Since the original example was for the top and bottom edges of the images in an axial study results, i.e., a plane oriented in xz, the solution for this example will follow that case. Note that $\bar{y_i}$ can be calculated using the ideal plane. Since with proper orientation of the cube the distortion for this face is essentially all in the y direction, the ideal x and z coordinates ($\bar{x_i}$ and $\bar{z_i}$) are assumed to be the same as the distorted (x_i and z_i).

$$\begin{aligned} C_c \pm \delta\|N\| &= N^T p_{ideal} \\ &= \begin{bmatrix} -C_x \\ 1 \\ -C_z \end{bmatrix}^T \begin{bmatrix} x_i \\ \bar{y_i} \\ z_i \end{bmatrix}^T \\ C_c \pm \delta\|N\| + C_x x_i + C_z z_i &= \bar{y_i} \end{aligned} \tag{5}$$

Knowing the ideal point $(\bar{x_i}, \bar{y_i}, \bar{z_i})$ and the distorted points (x_i, y_i, z_i), substitute into the spherical harmonics expansion and note the linearity in the K terms. Using all n points of both planes oriented in the xz direction yields:

$$TK_y = \Delta Y \tag{6}$$

where,

$$
\begin{aligned}
\Delta Y &= \begin{bmatrix}(y_0 - \bar{y_0}) & \cdots & (y_{2n-1} - \bar{y}_{2n-1})\end{bmatrix}^T \\
T &= \begin{bmatrix} T_{0,0} & \cdots & T_{0,4} \\ \vdots & \ddots & \vdots \\ T_{2n-1,0} & \cdots & T_{2n-1,4} \end{bmatrix} \\
& T_{i,0} = \bar{y_i}\left(\bar{x_i}^2 + \bar{y_i}^2\right) \\
& T_{i,1} = \bar{y_i}\left(\bar{z_i}^2\right) \\
& T_{i,2} = \bar{y_i}\left(\bar{x_i}^2 + \bar{y_i}^2\right)\bar{z_i}^2 \\
& T_{i,3} = \bar{y_i}\left(\bar{x_i}^2 + \bar{y_i}^2\right)^2 \\
& T_{i,4} = \bar{y_i}\left(\bar{z_i}^4\right) \\
K_y &= \begin{bmatrix}K_{y_0} & \cdots & K_{y_4}\end{bmatrix}^T
\end{aligned}
$$

Solving for K_y was accomplished using linear least squares by QR factorization (Matlab "\" operator). This process was repeated for the other distortion parameters K_x and K_z. Once the distortion parameters were obtained, they were applied to MR images of the performance study, described below.

3 Results and Discussion

3.1 Performance Study

The performance of the distortion correction code was tested by localizing the 20 markers in the Lucy® phantom, which had known stereotactic coordinates derived from precision dimensional inspection. The corrected locations of the markers were compared to the measured physical locations. This step required performing a *stereotactic transformation*, to convert the coordinates in the images to a stereotactic coordinate system created by the fiducial points on the attached stereotactic frame. Target localization was performed in two ways: The first method obtained the coordinates of the MRI fiducial points and marker points (Figure 2) from the distorted images and their corrected positions were calculated by iteratively solving Eq. 4 using the *minerr* function of Mathcad version 13. The corrected fiducial marker coordinates were then processed by a custom stereotactic localization program written in Mathcad and the parameters of a 3D stereotactic transformation (rotation matrix and translation vector) were obtained according to the algorithm described in [8]. The second method processed the entire MR image set in the following way. Starting with an empty voxel grid of identical size to the original study, the location of each voxel in the distorted space was calculated according to Eq. 4 and the mean MRI signal intensity from nearest voxel neighbors to the distorted voxel location was calculated and assigned to the undistorted voxel location. This way, the entire undistorted image space was rebuilt. The distortion-corrected MRI set was then read into Odyssey® (PerMedics, Inc.), a commercially-available radiation treatment planning system, and the built-in stereotactic localization feature of Odyssey® was used to determine the stereotactic marker coordinates. Both methods gave similar results within voxel accuracy.

The *localization error*, defined as the x, y, and z components of the vector between the MRI-determined and the metrology-lab measured marker locations was determined for three scenarios: (1) error associated with our phantom-based MRI gradient nonlinearity distortion correction, (2) error when no correction was performed, and (3) error associated with a built-in internal scanner correction method for gradient field non-linearities. The latter feature was turned off for the first two scenarios.

3.2 Numerical Results

Figure 6 demonstrates the mean and standard deviation of the localization error of the 20 MRI markers. Localizing the markers without any distortion correction resulted in stereotactic localization errors typically between 1.0mm and 2.0mm. This accuracy decreased greatly with increasing Z-offset from gradient isocenter, with errors reaching nearly 3.0mm. At gradient isocenter, the internal correction yielded accuracies better than 1.0mm, but was insufficient in providing this quality at $\pm$50mm Z-offset. In contrast, the phantom-based MRI gradient nonlinearity distortion correction provided consistent submillimeter accuracy in all test cases, even for $\pm$50mm $Z-$offset. Considering the worst case, the correction method yielded accuracies of approximately 0.6 ± 0.3mm. In the best case, the phantom-based MRI gradient nonlinearity distortion correction reduced localization error to nearly 0.0 ± 0.3mm. Considering each scan image, these values correlated to approximately one pixel in the worst case, and to $\frac{1}{2}$ pixel in the best case.

4 Conclusions

Our results confirm that correcting gradient nonlinearity distortion-a primary source of distortion in MRI-brings the accuracy in MRI-based stereotactic localization into the submillimeter domain. Without any correction the error typically exceeds 1.0mm and can reach up to 3.0mm. Our correction method provided consistent submillimeter accuracy in localizing the targeting markers even when the object was $\pm$50 mm off isocenter, while the internal correction method did not consistently provide submillimeter accuracy .

5 Current and Future Work

5.1 Scanner and Phantom

Up to this point we have only tested our method with one scanner model (Siemens VISION). Several new 3T MRI scanner models (GE and Siemens) will be utilized

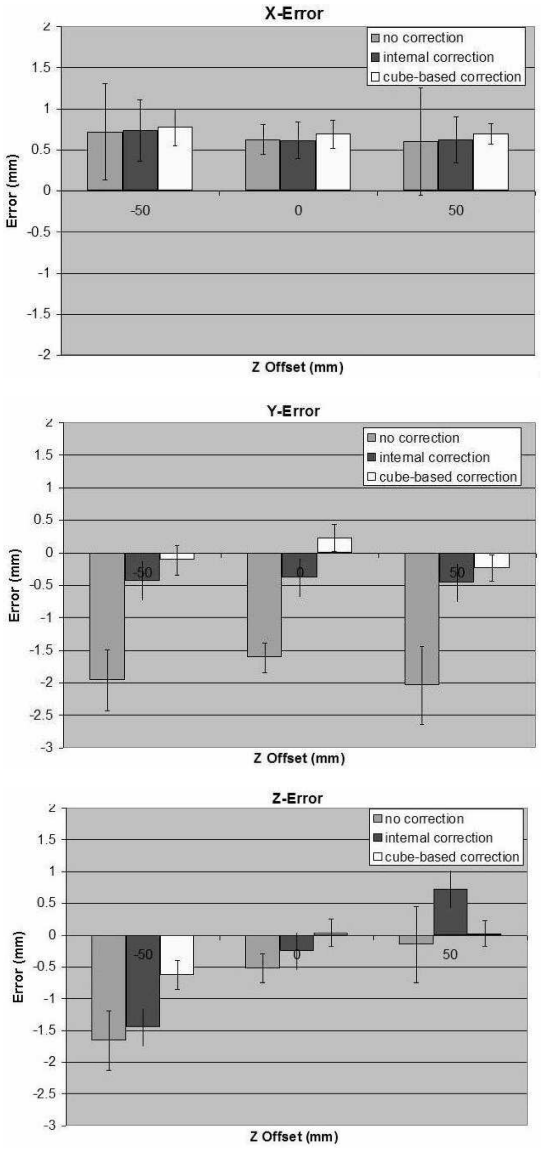

Figure 6: Stereotactic localization error of 20 markers with respect to each coordinate axis, with and without distortion correction.

for further testing, to confirm the correction model is valid for both the different scanner and the stronger magnetic field. Since the existing cube phantom is relatively limited in size and the fiducial points of the MR indicator are up to 10 beyond the cube surfaces, we are contemplating the use of a larger cube phantom (30cm side length) for more accurate distortion modeling.

In this work, we have assumed that the gradient isocenter coincides with the origin of the MRI-based coordinate system as specified by the DICOM header, which may not be always the case. In discussions with the vendor of the tested scanner, we were informed that the exact location of the gradient isocenter is not known. Assuming the gradient isocenter at the wrong location compromises the accuracy of the distortion correction model. In future, work it is planned to including the unknown location of the gradient isocenter in the distortion model and finding its position using a least square fitting routine.

5.2 GPGPU

Although the gradient nonlinearity distortion correction has demonstrated its effectiveness, the speed at which the calculations are performed is quite slow. On average, this Matlab program requires 20-30 minutes to execute on a typical PC. While this is not a ridiculous amount of time, reducing the computation time to minutes or even seconds will greatly increase the effectiveness and feasibility of utilizing the software in a clinical environment.

To significantly reduce the computation time of the MRI gradient nonlinearity distortion correction method, specific portions of the software will be converted to use *General-Purpose Computing on Graphics Processing Units (GPGPU)* techniques. Current GPU hardware is specialized for compute-intensive, highly parallel computation, thereby allowing the GPU to attain nearly 500 GFLOPS, compared to 40 GFLOPS for current high-end desktop CPUs [9]. Typical achieved speedup with modern GPU hardware is 100× or more on typical compiled programs [10]. With an increasing number of scientists and engineers utilizing GPU hardware for medical applications, especially CT [11, 12, 13], we believe that the same techniques can also be applied to our MRI distortion correction method. We are currently evaluating hardware and software from NVIDIA. NVIDIA provides a free SDK and toolkit called *CUDA*, which stands for *Compute Unified Device Architecture*. CUDA allows issuing and managing of computations on the GPU as a data-parallel computing device without the need of mapping them to a graphics API [9]. CUDA is an extension to the C programming language, and therefore does not require a steep learning curve. This will aid in our development of a GPU-accelerated software-based MRI gradient nonlinearity distortion correction. CUDA is available for the NVIDIA GeForce 8, 9, and 200 Series GPUs, all of which are easily obtainable and very affordable families of GPU hardware. Compatible GPUs can be purchased at nearly any computer retailer for as little as $30. Accelerating this distortion correction method with GPU hardware will yield great performance gains. Since Matlab is a scripting language, computational performance is quite limited. Merely converting from Matlab to a compiled language such as C will yield 50× speedup [7]. According to other literature, accelerating the compiled C code using GPGPU techniques can yield an additional 100× speedup or more [9]. Combining the two together-converting the Matlab code to C with portions accelerated on GPUs-can yield nearly 500× speedup, or more. Rather than waiting 20-30 minutes, the GPU-accelerated implementation could yield results in as little as 2.4-3.6 seconds. Even though these performance values are estimated, obtaining this level of performance is not unrea-

sonable, when considering the results shown in our past research [7], as well as currently published GPGPU applications [9, 10, 11, 12, 13].

References

[1] D. Kondziolka, *Functional Radiosurgery,* Neurosurgery, vol. 44, pp. 12-20, 1999.

[2] S.J. Doran, L. Charles-Edwards, S.A. Reinsberg, and M.O. Leach MO, *A Complete Distortion Correction for MR Images: I. Gradient Warp Correction,* Phys. Med. Biol., vol. 50, pp. 1343-1361, 2005.

[3] D. Wang, W. Strugnell, G. Cowin, D.M. Doddrell, and R. Slaughter, *Geometric Distortion in Clinical MRI Systems Part II: Correction Using a 3D Phantom,* J. Magn. Reson. Imaging, vol. 22, pp. 1223-1232, 2004.

[4] S. Langlois, M. Desvignes, J.M. Constans, and M. Revenu, *MRI Geometric Distortion: A Simple Approach to Correcting the Effects of Non-linear Gradient Fields,* J. Magn. Reson. Imaging, vol. 9, pp. 821-831, 1999.

[5] Lee, T.S., Schubert, K.E., and Schulte, R.W. *Software Development for Correction of Gradient-Nonlinearity Distortions in MR Images.* Proceedings of the International Conference on Computer Science and its Applications, June 2006, pp. 275-9.

[6] Lee, T.S., Schubert, K.E., and Schulte, R.W. *Gradient Non-Linearity Correction of MR Images for Functional Radiosurgery.* Proceedings of the International Conference on Computer and Information Science, July 2006, pp. 338-43.

[7] Lee, T.S. *Software-Based Gradient Nonlinearity Distortion Correction.* MSc Thesis, California State University San Bernardino, December 2006.

[8] K. Weaver, V. Smith, J.D. Lewis, B. Lulu, C.M. Barnett, S.A. Leibel, P. Gutin, D. Larson, and T. Phillips, *A CT-based computerized treatment Planning system for I-125 stereotactic brain implants* Int. J. Radiation Oncology Biol. Phys. vol. 18, pp. 445-454, 1990.

[9] NVIDIA Corp. *CUDA Compute Unified Device Architecture: Programming Guide.* v1.1, 2007.

[10] Luebke, David. *High Performance Computing with CUDA.* SUPERCOMPUTING 2007 Presentation, November 2007.

[11] H. Scherl, B. Keck, M. Kowarschik, and J. Hornegger. *Fast GPU-Based CT Reconstruction using CUDA.* Nuclear Science Symposium Conference Record, Vol. 6, 4464-4466, 2007.

[12] K. Mueller, F. Xu, and N. Neophytou, *Why Do Commodity Graphics Hardware Boards (GPUs) Work So Well for Acceleration of Computed Tomography?* in SPIE Electronic Imaging Conference, San Diego, 2007, (Keynote, Computational Imaging V).

[13] N. Neophytou, F. Xu, and K. Mueller. *Hardware Acceleration vs. Algorithmic Acceleration: Can GPU-Based Processing Beat Complexity Optimization for CT?* SPIE Medical Imaging '07, San Diego, 2007.